
Article:
Calabrese, V., György, C., Haward, S.J. et al. (2022) Microstructural dynamics and rheology of worm-like diblock copolymer nanoparticle dispersions under a simple shear and a planar extensional flow. Macromolecules, 55 (22). pp. 10031-10042. ISSN: 0024-9297

https://doi.org/10.1021/acs.macromol.2c01314

Macromolecules

pubs.acs.org/Macromolecules

Article

Microstructural Dynamics and Rheology of Worm-like Diblock Copolymer Nanoparticle Dispersions under a Simple Shear and a Planar Extensional Flow

Vincenzo Calabrese,* Csilla György, Simon J. Haward, Thomas J. Neal, Steven P. Armes, and Amy Q. Shen*

Cite This: *Macromolecules* 2022, 55, 10031−10042

Read Online

ACCESS | Metrics & More | Article Recommendations | Supporting Information

ABSTRACT: We investigate the shear and extensional flow behavior of dispersions composed of two types of worm-like nanoparticles (WLNPs) with comparable cross-sectional diameters, similar persistence lengths but differing contour lengths, and thus differing flexibility. By measuring the flow-induced birefringence (FIB) of WLNP dispersions in two contrasting microfluidic devices, we obtain an experimental quantification of the role of shearing and planar extensional flows at aligning a short and stiff WLNP (S-WLNP) and a relatively long and flexible WLNP (L-WLNP). We show that shear and extensional flows induce the alignment of both types of WLNPs. However, extensional deformations are more effective than shear deformations at triggering the onset of alignment of the WLNP. The difference between shear and extensional deformations for WLNP alignment is explained based on the ratio of extensional and shear viscosity of the solvent fluid (Trouton ratio of the solvent) and a structural parameter related to the WLNP extensibility and flexibility. Under shear flow, these WLNP dispersions display shear-thinning behavior, with an exponential reduction in viscosity with increasing alignment. Under extensional flow, the WLNP alignment leads to extensional thinning, making WLNP ideal additives for industrial and biotechnology formulations exposed to extensional dominated flows (e.g., jetting, spraying, and printing processes).

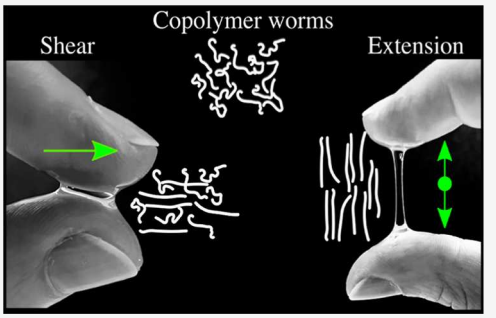

INTRODUCTION

Anisotropic colloidal objects with high aspect ratios are appealing materials from a scientific and industrial perspective. Compared to spherical particles, rod-like particles display complex phase behavior (e.g., the ability to form liquid crystalline phases),[1] lower percolation concentration,[2,3] a stronger increase in viscosity with increasing concentration, and the ability to adopt a preferential orientation under flow.[1,4] Colloidal dispersions under shear flow have been thoroughly investigated in the literature.[5] In comparison, extensional flows (i.e., uniaxial, biaxial, and planar) are less explored, despite playing a critical role in formulation performance and processability, as well as its undoubted importance for spraying, jetting, printing, and coating processes. Tactility and customer perception of cosmetic formulations are strongly connected with the extensional response of the fluid. For example, extensional-dominated flow can lead to "stringiness", which is undesirable for many cosmetic formulations (Figure 1a).[6] For Newtonian fluids, their shear viscosity (η) and the extensional viscosity (η_E) are related by the Trouton ratio (Tr) as $Tr = \eta_E/\eta$ with Tr depending on the type of extensional deformation (i.e., Tr = 3, 4, or 6 for uniaxial, planar, or biaxial extension, respectively).[7,8] The scenario is far more complicated for non-Newtonian fluids (including most colloidal dispersions and polymer solutions), for which their rheological response under extensional flows can drastically differ from that under shear flows (Figure 1b). For example, flexible polymer chains in solution exhibit an extensional viscosity that increases abruptly with the extension rate ($\dot{\varepsilon}$), while the shear viscosity is reduced with increasing shear rate ($\dot{\gamma}$) (see in Figure 1b).[9−13] Since rheological properties are usually linked to structural properties of the fluid, differing behavior observed under shear and extensional flow can be correlated with polymer conformations. Specifically, flexible polymer chains subjected to extensional flow undergo a so-called coil-to-stretch transition above a critical value of $\dot{\varepsilon}$.[14] On increasing $\dot{\varepsilon}$, the extensional viscosity η_E increases until maximum chain extension is attained, whereby η_E attains a plateau value that can be orders of magnitudes greater than the corresponding shear viscosity η (see Figure 1b). In contrast, flexible polymers preserve their coil-like structure under shear flow, thus the shear viscosity decreases with $\dot{\gamma}$ (shear-thinning behavior). This is a similar rheological response to that observed

Received: June 24, 2022
Revised: September 27, 2022
Published: October 18, 2022

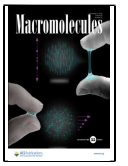

https://doi.org/10.1021/acs.macromol.2c01314
Macromolecules 2022, 55, 10031−10042

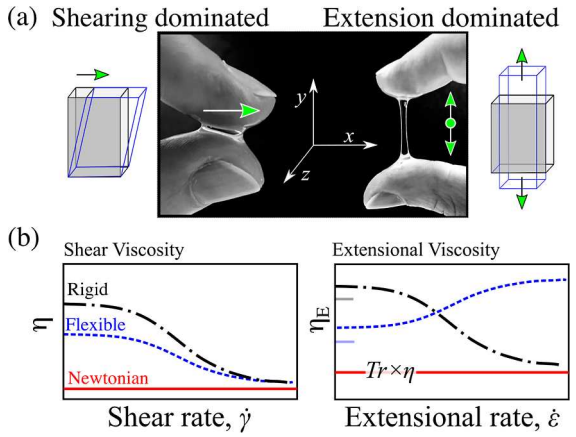

Figure 1. (a) Example of shear- and extensional-dominated deformations involved in the handling of a polymer-based formulation. Arrows indicate the direction of applied deformation. (b) Characteristic curves of shear viscosity (η) as a function of the shear rate ($\dot{\gamma}$) and extensional viscosity (η_E) as a function of the extensional rate ($\dot{\varepsilon}$) for three distinct fluids. Newtonian fluid (red), solution-containing flexible polymers (blue), and dispersion or solution-containing rigid rod-like structures (black) (e.g., colloidal rods and polyelectrolytes in solutions with low or zero salt).

for spherical colloidal particles.[5] Extended polymer chains (e.g., aqueous solutions of polyelectrolytes in the presence of low or zero salt concentrations) and rod-like colloids display similar trends of extensional and shear viscosity behavior with the respective rate of deformation,[9,15−18] largely due to the preferential structural alignment in the flow direction in both cases. Thus, the reported values of η_E for rod-like particles are relatively close to the respective η and rarely exceed $20 \times \eta$ for a given deformation rate.[13,16,18−20] The extent of flexibility of colloidal rod-like particles is expected to manifest through the differing rheological behavior of the dispersion under shear and extensional flows (see schematics Figure 1b).

Dispersions of rod-like particles have been thoroughly studied in rheometric shear flow because this is relatively easy to generate and control.[21] Rheo-optical techniques based on birefringence,[15,22−26] X-ray, and neutron scattering [e.g., rheo-small-angle scattering (rheo-SAS)][27−29] have been employed to link the structural and rheological behavior of colloidal dispersions under shear flow.[30,31] The effect of extensional flow on the structural properties of rod-like particle dispersions is often investigated in custom-built microfluidic platforms, such as contraction−expansion,[32] microfluidic cylinders,[16] flow focusing,[33] four-roll mill,[34] and cross-slot-type devices,[15,16] via light scattering and flow-induced birefringence (FIB) experiments. However, in most of these microfluidic platforms, the fluid elements do not undergo constant acceleration/deceleration to ensure a constant extensional rate $\dot{\varepsilon}$, which prevents quantitative comparison with the structural properties obtained under steady shear. Another matter of concern is the presence of both shear and extensional deformations generating the so-called "mixed flows", increasing the problem of isolating and studying the effect of extensional deformations. Given these experimental challenges, combined with the potential difficulty to control particle flexibility, it is not surprising that a quantitative comparison between the shear- and extensional-induced alignment for anisotropic particles of differing flexibility has not yet been reported in the literature.

To understand how the flexibility of rod-like colloids influences their alignment under shear and extension flows, we prepared two types of sterically stabilized diblock copolymer worm-like nanoparticles (WLNPs) with comparable cross-sectional diameters and similar persistence lengths but differing contour lengths and thus differing flexibility. More specifically, the behavior of short WLNP (S-WLNP) and relatively long WLNP (L-WLNP) dispersed in mineral oil is compared under shear and extensional flow by combining different rheometric techniques with bespoke microfluidic devices to retrieve rheological and structural information. We analyze the shear and extensional flow behavior of the S-WLNP and L-WLNP in the context of rigid rod-like particles and flexible polymers and demonstrate that controlling the WLNP morphology and flexibility enables rational design of the shear and extensional properties of the dispersions.

MATERIALS AND METHODS

Colloidal Dispersions of WLNPs. The WLNPs were prepared via polymerization-induced self-assembly in non-polar media.[35−37] More specifically, the reversible addition−fragmentation chain transfer (RAFT) dispersion polymerization of either methyl methacrylate (MMA) or benzyl methacrylate (BzMA) was conducted in mineral oil using a poly(stearyl methacrylate) (PSMA) precursor (see Scheme 1). In one case, relatively short $PSMA_{10}$-$PMMA_{83}$ WLNPs (the two

Scheme 1. (a) Synthesis of a Poly(stearyl methacrylate) ($PSMA_{10}$) Precursor via RAFT Solution Polymerization of SMA in Toluene at 50% w/w Solids Using 2-Cyano-2-propyl Benzodithioate (CPDB) at 70 °C (N.B. AIBN Denotes 2,2′-Azoisobutyronitrile); (b) RAFT Dispersion Polymerization of MMA at 20% w/w Solids in Mineral Oil Using *tert*-Butyl Peroxy-2-ethylhexanoate (T21s) Initiator at 90 °C; and (c) RAFT Dispersion Polymerization of Benzyl Methacrylate (BzMA) at 10% w/w Solids in Mineral Oil Using *tert*-Butyl Peroxy-2-ethylhexanoate (T21s) Initiator at 90 °C

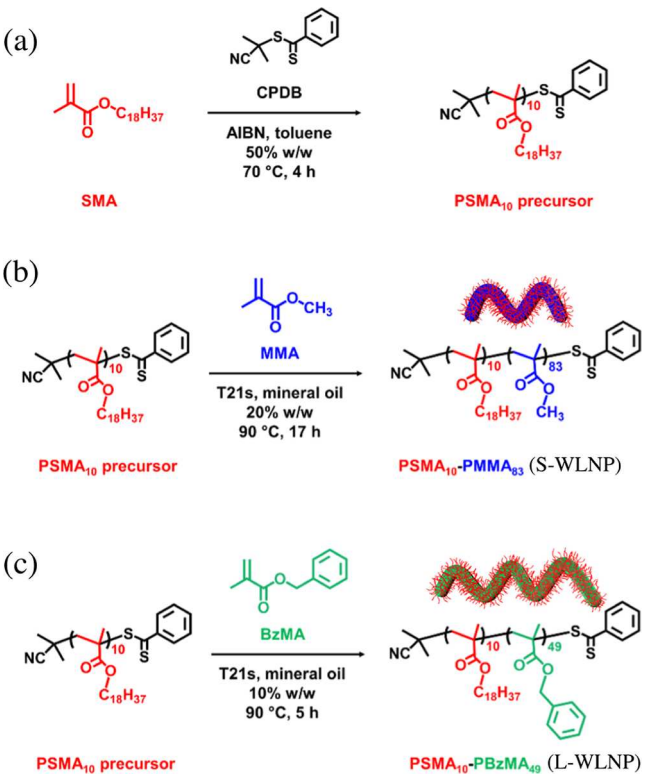

https://doi.org/10.1021/acs.macromol.2c01314
Macromolecules 2022, 55, 10031−10042

numerical subscripts refer to the mean degree of polymerization of each block) were obtained, which are denoted as S-WLNP (Scheme 1b). The second formulation produced relatively long $PSMA_{10}$-$PBzMA_{49}$ WLNPs, which are denoted as L-WLNP (Scheme 1c). The mineral oil was kindly provided by The Lubrizol Corporation Ltd., (Hazelwood, Derbyshire, UK). The MMA polymerization was quenched after 17 h at 90 °C, with ^{1}H NMR spectroscopy studies indicating more than 99% conversion (see the Supporting Information). Similarly, 97% conversion was achieved for the BzMA polymerization within 5 h at 90 °C. Gel permeation chromatography analysis indicated narrow molecular weight distributions ($M_w/M_n \leq 1.10$) for both diblock copolymers (see Figure S1 in the Supporting Information), suggesting that good RAFT control was achieved in each case. As indicated in Scheme 1, the $PMMA_{83}$ and $PBzMA_{49}$ chains are the oil-insoluble core-forming blocks of the S-WLNP and L-WLNP, respectively, while the $PSMA_{10}$ chains act as the oil-soluble steric stabilizer block for both types of WLNPs. A detailed description of each WLNP synthesis is provided in the Supporting Information.

Stock WLNP dispersions prepared directly in mineral oil were diluted with mineral oil to obtain a series of WLNP volume fractions (ϕ), where $\phi = V_{WLNP}/(V_{WLNP} + V_{solvent})$, where V_{WLNP} is the volume of the WLNP and $V_{solvent}$ is the volume of the mineral oil. All dispersions were prepared by gravimetry and stirred for at least 24 h after dilution to ensure homogeneity. V_{WLNP} and $V_{solvent}$ were calculated using densities of 8300, 1180, and 1150 (kg m^{-3}) for the mineral oil, S-WLNP, and L-WLNP, respectively. WLNP densities were estimated using the known solid-state densities of PMMA and PBzMA. All the WLNP dispersions were subjected to low magnetic stirring for at least 24 h prior to experiments. This protocol was required to ensure homogeneous, free-flowing dispersions. Indeed, if WLNP dispersions prepared at higher volume fractions were allowed to rest under zero-shear conditions, a free-standing gel was obtained after ca. 5 days owing to the formation of a 3D network comprising multiple interworm contacts.

Material Characterizations. *Transmission Electron Microscopy.* Transmission electron microscopy (TEM) studies were conducted using a Philips CM 100 instrument operating at 100 kV and equipped with a Gatan 1k CCD camera using a methodology previously described for similar block copolymer nanoparticles in mineral oil.[38,39] In brief, a single droplet of a 0.10% w/w WLNP dispersion was placed onto a carbon-coated copper grid and allowed to dry prior to exposure to ruthenium(VIII) oxide vapor for 7 min at 20 °C to improve the contrast for the core-forming block.[40]

Small-Angle X-ray Scattering. Small-angle X-ray scattering (SAXS) patterns were recorded for 1.0% w/w dispersions of S-WLNP and L-WLNP in mineral oil at a synchrotron source (ESRF, beamline ID02, Grenoble, France; experiment number SC-5109) using a monochromatic X-ray radiation of wavelength $\lambda = 0.0995$ nm and a Ravonix MX-170HS CCD detector. The scattering vector (q) is defined as $q = \sin(\tilde{\theta}/2)(4\pi/\lambda)$, where $\tilde{\theta}$ is the scattering angle. Each dispersion was placed in a glass capillary of 2 mm in diameter, and the scattering data were reduced using standard routines[41] and analyzed using Irena SAS macros in Igor Pro.[42]

Shear Rheometry. Rheological measurements were performed with a strain-controlled ARES-G2 rotational rheometer (TA Instruments Inc.) at 22 ± 0.1 °C controlled by a Peltier system (TA Instruments) using a stainless steel cone and plate geometry (50 mm in diameter and 1° cone angle). For each WLNP dispersion, the steady-state shear viscosity (η) as a function of the shear rate ($\dot{\gamma}$) was independent of the pre-shear protocol with no hysteresis observed during either increasing or decreasing shear rate ramps; this indicates negligible thixotropic effects on the time scale of a typical experiment (30−60 min). The frequency sweep was acquired at a constant strain amplitude, $\gamma_0 = 10\%$, which fell under the linear viscoelastic region. The storage modulus (G') and loss modulus (G'') were acquired as a function of the angular frequency (ω). The magnitude of complex modulus is computed as $|G^*| = (G'^2 + G''^2)^{1/2}$ and the magnitude of complex viscosity as $|\eta^*| = |G^*|/\omega$.

Uniaxial Extensional Rheometry. Uniaxial extensional rheometry was performed with the aid of a capillary breakup extensional rheometer (CaBER 1 Thermo Scientific) using the "slow retraction method" (SRM).[43] Briefly, the test fluid was loaded between two plates (6 mm in diameter) with an initial gap of ≈2 mm. To trigger the spontaneous filament thinning, the liquid filament was brought to its stability limit by slowly driving the bottom plate downward. The filament thinning was imaged with a high-speed camera (Phantom Miro M310, Vision Research Inc.) with a resolution of ≈24 μm/pixel at a rate of 4000 frames per second (fps) for the mineral oil and 2000 fps for the WLNP dispersions. The filament was backlit with white light (Dolan-Jenner Fiber-Lite Mi-LED A2). Using MATLAB, the image sequences were thresholded, converted to binary images, and the filament edge was tracked with the "Canny" edge function, in the given order. The evolution of the filament thinning over time could be monitored up to a minimum filament diameter of ≈100 μm. The surface tension (σ) of the samples was measured using a drop tensiometer with the pendant drop method (Attension Theta, Biolin Scientific). For the mineral oil used in this study, $\sigma = 30 \pm 1$ mN m^{-1}. The same σ value was obtained for the S-WLNP and L-WLNP dispersions.

Microfluidic Platforms for Shear Flow and Planar Extensional Flow. To generate a shear flow, we adopted a shearing flow-dominated channel (SFC, sketched in Figure 2a). The SFC is a straight rectangular channel with length $L = 25$ mm (along the x-axis), width $W = 0.4$ mm (along the y-axis), and height $H = 2.0$ mm (along the z-axis) and was fabricated as described previously.[15,44]

Planar extensional flows were generated using an optimized shape cross-slot extensional rheometer (OSCER, sketched in Figure 2b); a detailed description can be found in prior work.[11,45] Briefly, the OSCER has two incoming and two outgoing flows placed orthogonal to each other, generating a stagnation point at the center of symmetry ($x = y = 0$ mm). The OSCER has a height $H = 2.1$ mm and width $W = 0.2$ mm at the inlets and outlets. Within a large region around the stagnation point ($|x|, |y| \leq 7.5W$), the OSCER generates a steady planar extensional flow with negligible shearing contribution.[11,45] The SFC and OSCER devices have a relatively high aspect ratio ($H/W \geq 5$), ensuring negligible shear effects from the top and bottom walls and providing a good approximation to a 2D flow.[46]

Teflon tubing was used to connect the microfluidics platforms to Hamilton Gastight syringes. Nemesys low-pressure syringe pumps (CETONI, GmbH) were used to simultaneously infuse and withdraw the fluid at an equal and opposite volumetric rate, Q (m^3 s^{-1}), from inlet(s) and outlet(s), respectively, generating a mean flow velocity $|U| = Q/(WH)$ (m s^{-1}). In both geometries, creeping flow conditions were ensured at all tested flow rates by low values of the Reynolds number ($Re = \rho UW/\eta < 1$). The Re was estimated from density of the mineral oil ($\rho = 830$ kg m^{-3}), and η as the viscosity of the dispersion at $\dot{\gamma} = 100$ s^{-1} obtained from shear rheometry.

Pressure Measurement for Extensional Rheology. For the flow in the OSCER geometry, a 15 psi differential pressure sensor (Omega Engineering, Inc., CT, USA) was installed with a pressure port at an inlet (P_1) and a second pressure port at an outlet (P_2), see Figure 2b. The pressure difference, measured between the two pressure ports ($\Delta P = |P_1 - P_2|$), is evaluated in two distinct operating modes referred to as

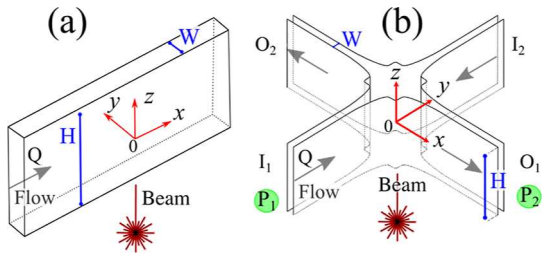

Figure 2. Schematic representation of the (a) shearing-flow dominated channel (SFC) and the (b) OSCER with respective coordinate systems. In (b), the inlets are marked by I_1 and I_2, while the outlets are marked by O_1 and O_2, with P_1 and P_2 indicating the location of the pressure ports of the differential pressure sensor. The beam indicates the position of the monochromatic light in the FIB experiment.

https://doi.org/10.1021/acs.macromol.2c01314
Macromolecules 2022, 55, 10031−10042

ΔP_{total} and ΔP_{shear}. ΔP_{total} was measured with both opposing inlets (I_1 and I_2, see Figure 2b) and outlets (O_1 and O_2) operating at equal and opposite flow rates so that planar extension generates around the stagnation point. The ΔP_{shear} was evaluated with only one inlet (I_1) and one outlet (O_1) operating at an equal and opposite flow rate, generating a shear-dominated flow that has no stagnation point.

Flow-Induced Birefringence. FIB measurements were performed in both SFC and OSCER, using an Exicor MicroImager (Hinds Instruments Inc.), employing a monochromatic light source with a wavelength of 450 nm. The microfluidic geometries were placed with their z-axis parallel to the light beam and imaged using a 5× objective lens (see Figure 2). For each flow rate, the flow was equilibrated for 5 ± 1 s. Subsequently, the retardance between the two orthogonally polarized light beams (R) and the orientation angle of the slow optical axis (θ) were obtained over a fixed time of 7 s using a stroboscopic illumination technique to perform Mueller matrix decomposition.[47] The birefringence is computed as $\Delta n = R/H$. The background value of Δn was obtained from the fluid at rest and subtracted from all measurements obtained under flow. The spatial resolution of the measurement was ≈2 μm/pixel. The FIB of the WLNP dispersions monitored over several flow cycles provided reproducible results, suggesting negligible cleavage of the WLNP under such experimental conditions.

RESULTS

WLNP Characterization. The WLNP dimensions were characterized by combining SAXS and TEM analyses (Figure 3). SAXS patterns for the WLNP dispersions were recorded at $\phi = 7 \times 10^{-3}$ (equivalent to 1.0% w/w, Figure 3a). In the low-q regime ($q < 0.04$ nm^{-1}), the scattering intensity, $I(q)$, does not approach a plateau (Guinier region), indicating that the accessible q-range is insufficient to enable the determination of the mean worm contour length (l_c). Therefore, the volume-weighted contour length, $\langle l_c \rangle$, was estimated by the analysis of more than 300 individual WLNP from TEM images using the so-called De Brouckere mean, which is expressed as

$$\langle l_c \rangle = \frac{\sum n_i l_{ci}^4}{\sum n_i l_{ci}^3} \quad (1)$$

where n_i is the number of worms of contour length l_{ci}. Using this approach, $\langle l_c \rangle$ is calculated to be 700 and 256 nm for the L-WLNP and S-WLNP, respectively.

In the high-q regime ($q > 0.2$ nm^{-1}), the SAXS patterns contain information regarding the mean cross-sectional diameter (d) of the WLNP. Fitting the SAXS patterns to a worm-like micelle model[48] (see the solid line in Figure 3a) yielded $d = 13.8 \pm 1.8$ nm and $d = 13.2 \pm 1.6$ nm for the S-WLNP and L-WLNP, respectively.

At intermediate q ($0.04 < q < 0.2$ nm^{-1}, see the highlighted box in Figure 3a), the scattering intensity for both WLNP dispersions follows the scaling relation $I(q) \propto q^{-1}$, which indicates a predominantly rod-like structure at length scales ($l = 2\pi/q$) in the range of $31.4 < l < 157$ nm. From imaging analysis of the TEM images, a persistence length $l_p \approx 50$ nm was obtained for both WLNP species using the mean-squared end-to-end distance (MSED) method for a worm-like chain model within the FiberApp routine (details in Usov and Mezzenga[49]). The l_p value indicates the segment length below which the WLNPs behave as rigid rods. For both WLNP species, $l_p \approx 50$ nm; thus, $\langle l_c \rangle / l_p$ is 14 and 5 for the L-WLNP and S-WLNP, respectively. In summary, both WLNPs can be classified as semiflexible nanoparticles as l_p and $\langle l_c \rangle$ share a similar length scale, with the L-WLNP being significantly more flexible than the S-WLNP.[4,50]

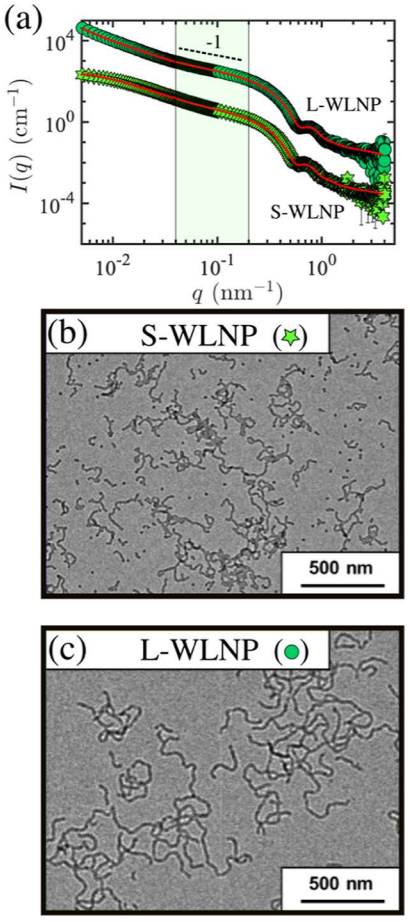

Figure 3. (a) SAXS patterns obtained at 20 °C for the S-WLNP (stars) and L-WLNP (circles) dispersed in mineral oil at $\phi = 7 \times 10^{-3}$ (1.0% w/w). The solid lines are fits to a worm-like micelle model,[48] while the dashed line indicates a q^{-1} slope. The L-WLNP curve is shifted upward (100×) for clarity. Representative TEM images obtained for (b) S-WLNP and (c) L-WLNP.

Shear Rheology. *Steady Shear Viscosity.* We begin by comparing the rheological response of the S-WLNP and L-WLNP under steady shear flow as a function of shear rate ($\dot{\gamma}$) over a wide range of volume fractions, ϕ (Figure 4). At low ϕ, both WLNP dispersions display a Newtonian-like shear viscosity, where η is almost independent of $\dot{\gamma}$ (Figure 4a,b). With increasing ϕ, these dispersions progressively display a shear-thinning behavior (reduction in η with increasing $\dot{\gamma}$), which is generally observed for elongated colloids[4,51] and soluble polymer solutions in the semidilute regime.[52−54] For rod-like colloidal dispersions, shear-thinning is associated with the increasing extent of rod alignment with increasing $\dot{\gamma}$, which results in reduced flow resistance.[4,28] Figure 4a,b shows that for each concentration, the steady shear viscosity, $\eta(\dot{\gamma})$ in filled symbols, overlays with the magnitude of complex viscosity, $|\eta^*|(\omega)$ in open symbols, obtained from the oscillatory test. This observation implies that the empirical Cox−Merz rule, stating that $\eta(\dot{\gamma}) = |\eta^*(\omega)|_{\dot{\gamma}=\omega}$, holds fairly well, as found for many viscoelastic fluids.[55,56] For rod-like colloidal dispersions, deviation from the Cox−Merz rule has been linked to the formation of a liquid crystalline phase.[57,58] This suggests that the concentrations of the WLNP dispersions investigated here are below the critical concentration required for the isotropic-to-

https://doi.org/10.1021/acs.macromol.2c01314
Macromolecules 2022, 55, 10031−10042

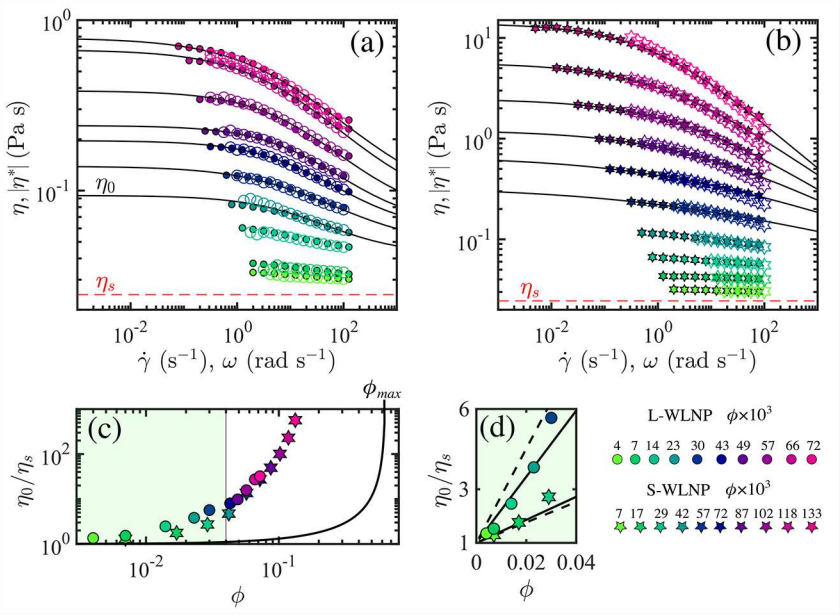

Figure 4. (a,b) Steady shear viscosity, η, as a function of the shear rate, $\dot{\gamma}$, (filled symbols) and the magnitude of complex viscosity, $|\eta^*|$, as a function of the angular frequency, ω, (empty symbols) for the L-WLNP in (a) and S-WLNP in (b), at various volume fractions, ϕ. Solid lines in (a,b) describe the fit (eq 2). (c) Normalized zero-shear viscosity η_0/η_s as a function of ϕ, where η_s is the solvent viscosity. The solid line represents the Krieger–Dougherty relationship for hard spheres. (d) Linear plot of η_0/η_s vs ϕ. Dashed lines are the plot of eq 4 using values of $[\eta]$ based on the Simha relationship (eq 5), considering the WLNP aspect ratio f retrieved from SAXS and TEM characterization, while the solid lines are the fits obtained using eq 4.

nematic transition. The absence of any nematic domains was also confirmed by performing birefringence experiments at rest.

The shear viscosity of the WLNP dispersions is well captured by the Cross model[59]

$$\eta = \eta_\infty + \frac{\eta_0 - \eta_\infty}{[1 + (\dot{\gamma}/\dot{\gamma}^*)^n]} \tag{2}$$

where η_0 is the zero-shear rate viscosity (low shear plateau), η_∞ is the infinite shear rate viscosity (high shear plateau), $\dot{\gamma}^*$ is the characteristic shear rate for the onset of shear thinning, and n is the power law exponent describing the shear-thinning region (results from the cross-model fit are provided in Tables S2 and S3, Supporting Information). At relatively high ϕ, both WLNP dispersions (Figure 4a,b) display a limiting viscosity at low values of $\dot{\gamma}$ (η_0). However, in all cases, the viscosity plateau at high shear rates, indicative of η_∞, lies outside our experimental window. Thus, to fit eq 2, we use the values of η_∞ from the prediction by Dhont and Briels for rigid rods, computed as[60]

$$\eta_\infty = \eta_s\left[1 + \left(\frac{2(\langle l_c\rangle/d)^2\phi}{45\ \ln(\langle l_c\rangle/d)}\right)\right] \tag{3}$$

where η_s is the solvent viscosity (see Tables S2 and S3 in the Supporting Information for values of η_∞).

To compare the shear rheology behavior exhibited by L-WLNP and S-WLNP dispersions, we plot the values of η_0 obtained from the cross model, normalized by η_s, as a function of the respective ϕ, see Figure 4c. For the lowest WLNP concentrations where the cross-model fit is omitted, the value of η_0 corresponds to that for η at the lowest accessible shear rate. Both WLNP dispersions (circle and star symbols) display a similar increase in viscosity as a function of ϕ. However, the L-WLNP leads to higher viscosity for a given volume fraction than the S-WLNP. This observation is consistent with the higher aspect ratio observed for the L-WLNP. For comparison, we plot in Figure 4c the expected increase in viscosity as a function of ϕ for dispersions of hard spheres as given by the Krieger–Dougherty (KD) relationship, $\eta_0/\eta_s = (1 - \phi/\phi_{max})^{-[\eta]\phi_{max}}$, by using an intrinsic viscosity $[\eta] = 2.5$ and a maximum volume fraction $\phi_{max} = 0.63$ (for random close packing).[5,61−63] As expected, the elongated WLNPs give rise to a significantly stronger increase in shear viscosity compared to such hard sphere dispersions. From the linear increase in viscosity for small ϕ ($\phi \to 0$) (Figure 4d), the intrinsic viscosity, $[\eta]$, for the WLNP can be obtained as

$$\frac{\eta_0}{\eta_s} = 1 + [\eta]\phi \tag{4}$$

The Simha relation for rigid rod-like particles provides an estimate of $[\eta]$ by knowing the particle aspect ratio ($f = l_c/d$) as[64]

$$[\eta] = \frac{f^2}{15(\ln\ 2f - 1.5)} + \frac{f^2}{5(\ln 2f - 0.5)} + \frac{14}{15} \tag{5}$$

Based on the SAXS and TEM characterizations, the particle aspect ratio is $f \equiv \langle l_c\rangle/d \approx 50$ and $\approx$20 for the L-WLNP and S-WLNP, respectively. These values of f yield the prediction of $[\eta] = 176$ and $[\eta] = 38$ for the L-WLNP and S-WLNP, respectively, based on eq 5, that capture the trend of η_0/η_s at $\phi \to 0$ closely (see the dashed lines, in Figure 4d).

Alternatively, using eq 4 to fit the data in Figure 4d, we obtain an experimental assessment of $[\eta]$ and f (from eq 5). Following this procedure, $f = 40.6$ (based on $[\eta] = 123$, solid line) for the L-WLNP, whereas $f = 21.5$ (based on $[\eta] = 43$, solid line) for the S-WLNP. These $f \equiv \langle l_c\rangle/d$ values are consistent with the SAXS and TEM data, whereby $\langle l_c\rangle/d \approx 50$ and $\approx$20 for the L-WLNP and S-WLNP, respectively. It is important to note that the f value

https://doi.org/10.1021/acs.macromol.2c01314
Macromolecules 2022, 55, 10031−10042

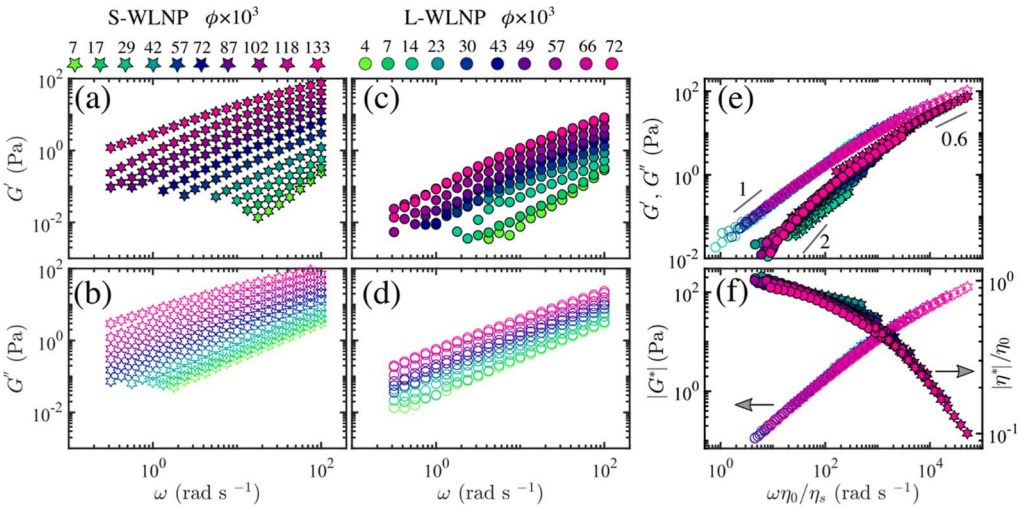

Figure 5. (a–d) G' (filled symbols) and G'' (open symbols) as a function of the angular frequency, ω, for the S-WLNP in (a,b) and L-WLNP in (c,d) for different volume fractions, ϕ. (e,f) Time–concentration superposition for the S-WLNP and L-WLNP at $\phi > \phi^*$. (e) G' and G'' vs the scaled frequency ($\omega\eta_0/\eta_s$). (f) $|G^*|$ and $|\eta^*|/\eta_0$ vs $\omega\eta_0/\eta_s$. The master curves in (e,f) are constructed from 16 different data sets.

obtained by the Simha relation is retrieved from the zero-shear viscosity, η_0, which probes the hydrodynamic dimension of such nanoparticles in their equilibrium conformation. Thus, for flexible anisotropic nanoparticles that can coil up in the absence of flow, f is expected to underestimate the "real" aspect ratio as determined by TEM analysis.[65]

Finally, the WLNP overlap concentration, indicating the transition from the dilute to the semi-dilute regime, can be estimated, using $[\eta]$ obtained from the fit of eq 4, as $\phi^* \approx [\eta]^{-1}$, yielding $\phi^* \approx 8 \times 10^{-3}$ (≈1.1% w/w) and $\phi^* \approx 23 \times 10^{-3}$ (≈3.0% w/w) for the L-WLNP and S-WLNP, respectively.

Oscillatory Shear Rheology. In Figure 5a–d, we present the storage (G', filled symbols) and loss (G'', open symbols) modulus as a function of angular frequency (ω), as obtained from oscillatory shear rheology studies of the WLNP dispersions. We find $G' < G''$ at all concentrations and frequencies examined, which indicates a viscous-dominated response. Interestingly, for all concentrations examined within the semi-dilute regime ($\phi > \phi^*$), the G'' trends for the L-WLNP and S-WLNP are self-similar and could be superimposed onto master curves (Figure 5e) by simply scaling the frequency as $\omega\eta_0/\eta_s$ using the normalized zero-shear viscosity (η_0/η_s) obtained from the steady shear measurements (see Figure 4c). In contrast, the data collapse is much less satisfactory for G', with this discrepancy becoming more evident when plotting $\tan\delta = G''/G'$ as a function of the scaled frequency (see Figure S2 in the Supporting Information). By analogy to the well-known time–temperature superposition principle, the construction of master curves for G' and G'' at various concentrations using a scaled frequency is usually described as the time–concentration superposition (TCS) principle, which is expected to be valid for systems that share the same relaxation mechanism.[57,66] Although the data collapse for G' is imperfect, especially at low frequency, the G' and G'' master curves (Figure 5e) still provide a useful qualitative indication of the rheological behavior of the WLNP over a wide range of angular frequency not accessible from a single measurement at a fixed concentration.

At low frequencies, master curves reveal approximate $G'' \propto (\omega\eta_0/\eta_s)$ and $G' \propto (\omega\eta_0/\eta_s)^2$ scalings, as expected for viscoelastic liquids, whereas $G' \simeq G'' \propto (\omega\eta_0/\eta_s)^{0.6}$ at high frequency.[52,67] Using the scaled frequency ($\omega\eta_0/\eta_s$), master curves for the magnitudes of complex modulus, $|G^*|$, and of normalized complex viscosity, $|\eta^*|/\eta_0$, could also be constructed (Figure 5f). This suggests that the L-WLNP and S-WLNP share the same relaxation mechanism in the semi-dilute regime. More specifically, as G'' provides a significantly better master curve, we infer that the L-WLNP and S-WLNP exhibit the same viscous relaxation behavior. For systems that share the same relaxation mechanism, the TCS principle is expected to remain valid when scaling the frequency as $\omega\tau$, where τ is the longest relaxation time of the colloidal particles. From the theory of rigid rods in the semi-dilute regime[4]

$$\eta_0/\eta_s \propto \phi^3 \text{ and } \tau \propto \phi^2 \tag{6}$$

thus $\eta_0/(\phi\eta_s) \propto \tau$. If the rigid-rod theory holds for the WLNP, then scaling the frequency as $\omega\eta_0/(\phi\eta_s)$ should provide more appropriate master curves with better superposition. Indeed, scaling the frequency as $\omega\eta_0/(\phi\eta_s)$ has been reported to be successful for the TCS of rigid rod-like particles.[57] However, in our case, the scaling $\omega\eta_0/\eta_s$ shown in Figure 5e,f works significantly better than the expected scaling for rigid rods, $\omega\eta_0/(\phi\eta_s)$. This suggests that $\eta_0 \propto \tau$ is more appropriate for the WLNP, rather than the $\eta_0/\phi \propto \tau$ relationship expected for rigid rods. Considering $\tau = \dot{\gamma}^{*-1}$ with $\dot{\gamma}^*$ obtained from the cross model (fit to steady flow curves in Figure 4a,b), the relationship $\eta_0 \propto \tau$ seems to be supported (see Figure S3 in the Supporting Information). Interestingly, the scaling relationship $\eta_0 \propto \tau$ has been reported experimentally for some semi-flexible polymer chains in solution.[68−71]

Extensional Rheology. *Uniaxial Extension.* We proceed by analyzing the rheological behavior of the WLNP dispersions in uniaxial extensional flow as generated by the capillary-driven thinning of a liquid filament. Snapshots of the filament thinning are given in Figure 6a at different times expressed as $t - t_0$, where t_0 is the time of filament breakup. We compare the evolution of the filament thinning of the L-WLNP and S-WLNP at $\phi = 66 \times 10^{-3}$ and $\phi = 72 \times 10^{-3}$, respectively, so as to have comparable shear viscosities $\eta_0 \simeq 0.07$ Pa s. Mineral oil with a constant viscosity $\eta = \eta_s = 24.5$ mPa s, which is the continuous phase for these WLNP dispersions, is used as a reference fluid. The L-WLNP and S-WLNP dispersions exhibit a similar thinning

https://doi.org/10.1021/acs.macromol.2c01314
Macromolecules 2022, 55, 10031−10042

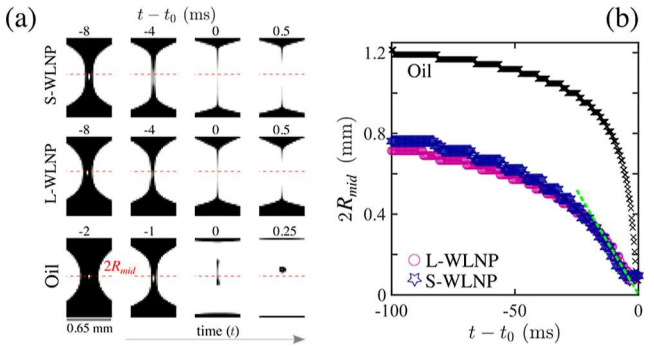

Figure 6. (a) Binary images of the capillary thinning over time ($t - t_0$) for the L-WLNP and S-WLNP dispersions at $\phi = 66 \times 10^{-3}$ and $\phi = 72 \times 10^{-3}$, respectively, with matched $\eta_0 \simeq 0.07$ Pa s, together with the mineral oil (solvent) as a reference. The dashed red line in (a) indicates the location where the filament radius at the mid-height (R_{mid}) is obtained. (b) Filament radius at the mid-height (R_{mid}) is plotted over time ($t - t_0$).

behavior (Figure 6a), with the fluid breaking at the middle point of the filament. Such behavior is characteristic of the viscocapillary regime.[43] The mineral oil displays substantially faster thinning compared to the WLNP dispersions, and the breakage occurs at the two extremities of the fluid filament, leading to the formation of a satellite droplet. In this case, the low viscosity of the mineral oil gives rise to high fluid velocities and inertia becomes dominant near the breakup time.[43,72] In Figure 6b, we compare the time evolution of the mid-height filament diameter, $2R_{mid}$ (tracked in the position of the dashed red line in Figure 6a). The L-WLNP and S-WLNP dispersions exhibit a similar reduction in the filament diameter over time, following a linear decrease near the breakup time (see the dashed line in Figure 6b). This is expected for viscous-dominated fluids because filament thinning is governed by the balance between the viscous and the surface tension force (viscocapillary regime). A similar linear dependence of the filament thinning over time has been observed for semi-dilute dispersions of anisotropic particles[17−19] and also for solutions of semi-flexible polymer chains.[9,73] In contrast, highly flexible polymer chains display a slower, exponential reduction in filament thinning over time. This is known as *elastocapillary* thinning, from which the relaxation time of the fluid can be calculated.[21] Unfortunately, in the absence of any measurable elastocapillary regime, we are unable to obtain relaxation times for the WLNP dispersions by the capillary thinning method.

The linear reduction in the filament diameter over time suggests that these WLNP dispersions do not exhibit extensional hardening.

From an industrial perspective, the presence of the WLNP in the mineral oil prevents the formation of satellite droplets without increasing the stringiness or stickiness of the fluid, making such WLNP an ideal additive for applications based on liquid handling (e.g., printing or jetting). Indeed, contamination by satellite droplets and long filament tails are problematic for applications that require rapid and clean dispensing of viscoelastic fluids.

Planar Extension. We evaluate the pressure drop within the OSCER device to retrieve information regarding the extensional rheology of the WLNP dispersions. The pressure drop is evaluated in two modes. The total pressure ΔP_{total} is measured with both opposing inlets (I_1 and I_2, see Figure 2b) and outlets (O_1 and O_2) operating at equal and opposite flow rates so that planar extension is generated around the stagnation point. The pressure of a shear-dominated flow without a stagnation point was evaluated with only one inlet (I_1) and one outlet (O_1) operating at a single constant and opposite flow rate and is referred to as ΔP_{shear}. In Figure 7, we present the pressure drop analysis for the L-WLNP and S-WLNP at $\phi = 66 \times 10^{-3}$ and $\phi = 72 \times 10^{-3}$, respectively, using mineral oil as a reference Newtonian fluid. We find that $\Delta P_{total} \simeq \Delta P_{shear}$ for the oil as well as for the L-WLNP and S-WLNP, indicating that the extensional stress contribution to ΔP_{total} is relatively small. The only difference between the three samples shown in Figure 7 is the slope of ΔP_{total} and ΔP_{shear} as a function of the mean flow velocity $|U|$. The mineral oil follows $\Delta P_{total} \simeq \Delta P_{shear} \propto U$ as expected for a Newtonian fluid, while for the L-WLNP and S-WLNP, $\Delta P_{total} \simeq \Delta P_{shear} \propto U^{0.8}$ and $\Delta P_{total} \simeq \Delta P_{shear} \propto U^{0.9}$, respectively, as expected for shear-thinning fluids.[74] In contrast to these WLNP results, flexible and semi-flexible polymer solutions exhibit a positive excess pressure drop such that $\Delta P_{excess} = (\Delta P_{total} - \Delta P_{shear}) > 0$, when used at flow rates above that required for the coil-to-stretch transition to occur, which is associated with the development of significant extensional stress within the stretched fluid.[9,11,75] Our uniaxial extension and planar extension results suggest that (i) the rheological properties in shear and extension are similar and (ii) the WLNP do not cause extensional hardening, as is commonly observed for solutions of flexible polymer chains.[21]

Flow-Induced Alignment: Shear and Planar Extension. To assess WLNP conformations under either shear or extensional flow, we use a SFC to generate a shearing deformation and an OSCER to generate planar extensional deformations around the stagnation point that are steady and shear free.[11,45] In Figure 8, we compare the birefringence for the L-WLNP and S-WLNP dispersions at $\phi = 66 \times 10^{-3}$ and $\phi = 72 \times 10^{-3}$, respectively. To account for these differing volume fractions, the birefringence intensity, Δn, is presented in normalized form as $\Delta n/\phi$. In the SFC and OSCER, the increase in mean velocity $|U|$ leads to a general increase in birefringence and, at comparable values of $|U|$, the L-WLNP always display stronger birefringence than the S-WLNP (note the different scale bar between the L-WLNP and S-WLNP in Figure 8). Analyzing the birefringence pattern in the SFC, it is clear that the

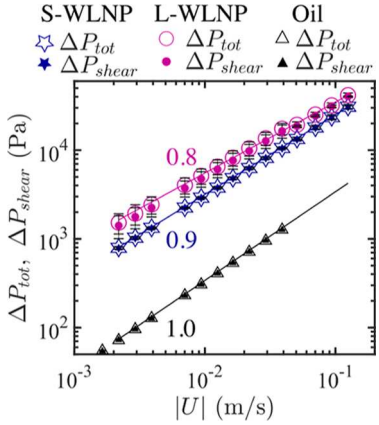

Figure 7. Pressure drop in shear (ΔP_{shear}) and in the presence of the stagnation point (ΔP_{total}) acquired in the OSCER device for the L-WLNP and S-WLNP dispersions at $\phi = 66 \times 10^{-3}$ and $\phi = 72 \times 10^{-3}$, respectively, with matched $\eta_0 \simeq 0.07$ Pa s, together with the mineral oil (solvent) as a reference.

https://doi.org/10.1021/acs.macromol.2c01314
Macromolecules 2022, 55, 10031−10042

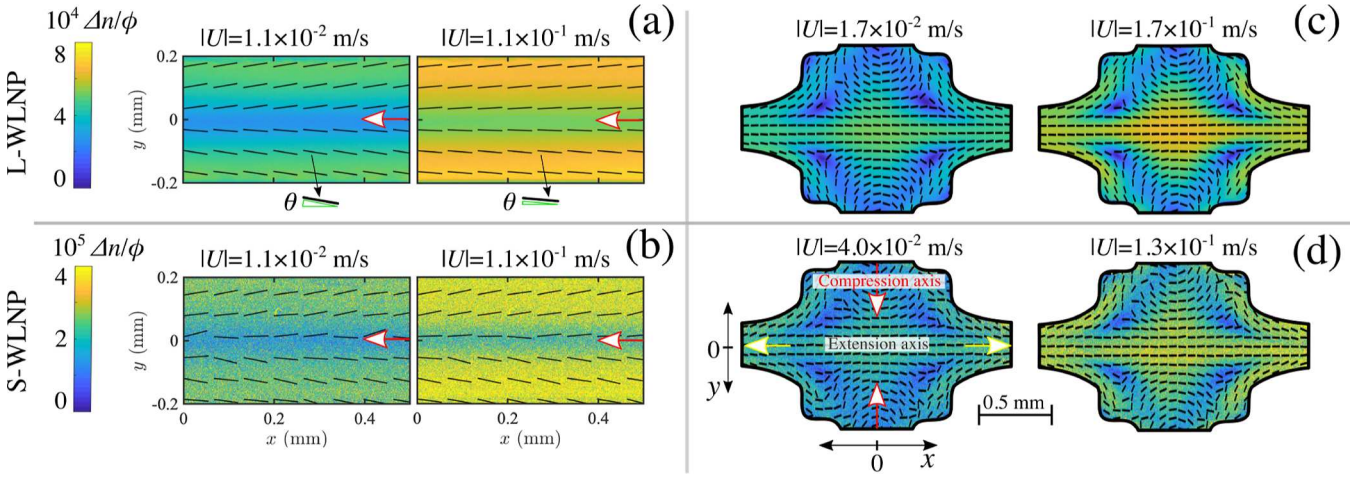

Figure 8. FIB at characteristic mean flow velocities $|U|$ for the SFC and OSCER. The L-WLNP [top row (a,c)] and S-WLNP [bottom row (b,d)] at $\phi = 66 \times 10^{-3}$ and $\phi = 72 \times 10^{-3}$, respectively. The normalized birefringence, $\Delta n/\phi$, is illustrated by the contour plot while the direction of the slow optical axis, θ, is indicated by the solid lines. The arrows indicate the flow directions.

most intense birefringence is obtained near the channel walls, where the velocity gradient along the y-axis reaches its maximum value. In contrast, birefringence is minimized close to the centerline (y = 0 mm), where $|\dot{\gamma}| \to 0$. Birefringence describes the extent of WLNP alignment and is expected to be proportional to the number of aligned l_p segments. Thus, near the channel walls of the SFC, a higher proportion of the WLNP segments is aligned when compared to the centerline. The solid lines projected onto the contour plot indicate the orientation angle of the slow optical axis (θ) with respect to the x-axis and reflect the WLNP orientation.[26] For the L-WLNP, the θ angle decreases significantly with increasing $|U|$, indicating that almost perfect parallel alignment to the flow direction can be achieved at high flow rates (see Figure 8a).[15,26,76]

In the OSCER, the fluid is compressed along the y-axis and extended along the x-axis (see the coordinate system in Figure 8d with arrows indicating the flow direction), generating a stagnation point at $x = y = 0$ mm. As the fluid moves away from the stagnation point along the x-axis, it is subjected to constant acceleration, resulting in a uniform extension rate, $|\dot{\varepsilon}|$.[15,74] The θ angle indicates that the WLNP align perpendicular to the flow along the compression axis (y-axis) and align parallel to the flow in the extensional axis (x-axis). Such perpendicular alignment in compression-dominated flows has been observed for various anisotropic colloidal particles[15,16,77,78] and also for worm-like micelles.[32] The pronounced alignment along the compression and extensional axes manifests as a diamond-like area of strong birefringence around the stagnation point. Above a critical value of $|\dot{\varepsilon}|$ required for the coil-to-stretch transition to occur, solutions of flexible polymer chains in similar cross-slot devices show a well-defined strand of strong birefringence along the extensional axis (i.e., the x-axis at y = 0 mm) with no birefringence being observed for a large area along the compression axis.[14,45,74,79−81] In contrast, rod-like nanoparticles align similarly under compression as under extension, generating a diamond-like area of intense birefringence around the stagnation point.[15] In summary, it appears that the WLNP behave much more like rigid rods than flexible polymer chains.

To obtain further quantitative insights regarding the WLNP alignment, we extract the mean values of Δn from specific locations of the SFC and OSCER and analyze these data with respect to the relevant deformation rate. For the SFC, the mean birefringence $\langle \Delta n \rangle$ is obtained at $y = \pm 0.1$ mm for a distance along the x-axis of 0.5 mm. For the OSCER, $\langle \Delta n \rangle$ is obtained within a region around the stagnation point that corresponds approximately to pure extensional flow, that is, at y = 0 mm along $-0.5 < x < 0.5$ mm. $\langle \Delta n \rangle$ is evaluated as a function of $|\dot{\gamma}|$ in the SFC and $|\dot{\varepsilon}|$ in the OSCER, respectively, where $|\dot{\gamma}| = 3.38|U|/W$ and $|\dot{\varepsilon}| = 0.21|U|/W$.[15,74] First, we note that the L-WLNPs are significantly more birefringent than the S-WLNP and that the extensional flow promotes the onset particle alignment at lower deformation rates when compared to the shearing flow, as indicated by the earlier onset of birefringence (Figure 9a). Inspecting Figure 9a, it is evident that $\langle \Delta n \rangle/\phi$ values increase in a similar fashion for $|\dot{\gamma}|$ and $|\dot{\varepsilon}|$ for both L-WLNP and S-WLNP, which suggests that an analogous flow-induced structural mechanism operates in each case (Figure 9a). Based on experimental observations for non-interacting rigid rods ($\phi < \phi^*$), Calabrese et al.[15] suggested that the birefringence at identical values of $|\dot{\gamma}|$ and $|\dot{\varepsilon}|$ is equivalent when accounting for the Trouton ratio of the Newtonian solvent (Tr_s) as a scaling factor, specifically as

$$\Delta n(|\dot{\gamma}|) = \Delta n(\mathrm{Tr}_s|\dot{\varepsilon}|)|_{|\dot{\gamma}|=|\dot{\varepsilon}|} \tag{7}$$

where Tr_s depends only on the type of extensional deformation (Tr_s = 3, 4, or 6 for uniaxial, planar, or biaxial extension, respectively).[8] Equation 7 was proposed based on the hypothesis that rigid colloidal rods experiencing a pure extensional flow perceive the extensional viscosity of the solvent fluid, rather than the shear viscosity. The WLNPs investigated herein lie within a concentration regime where interparticle interactions occur ($\phi > \phi^*$), and their shape diverges from rigid rods. Thus, eq 7 is no longer expected to be valid. As our purpose is to experimentally test the formal identity of Δn under shear and planar extensional flow, we modified eq 7 to capture the deviation from the non-interacting rigid rods by incorporating a dimensionless scaling parameter α in eq 7 such that

$$\Delta n(|\dot{\gamma}|) = \Delta n(\alpha \mathrm{Tr}_s|\dot{\varepsilon}|)|_{|\dot{\gamma}|=|\dot{\varepsilon}|} \tag{8}$$

For non-interacting rigid rods, α = 1, whereas $\alpha > 1$ indicates deviation from such behavior. The birefringence data can be collapsed onto single master curves by scaling $|\dot{\varepsilon}|$ by ($\alpha \mathrm{Tr}_s$) (eq 8) with $\alpha \approx 2.4$ and $\alpha \approx 1$, for the L-WLNP and S-WLNP, respectively, and Tr_s = 4 (for planar extension) as shown in a

https://doi.org/10.1021/acs.macromol.2c01314
Macromolecules 2022, 55, 10031−10042

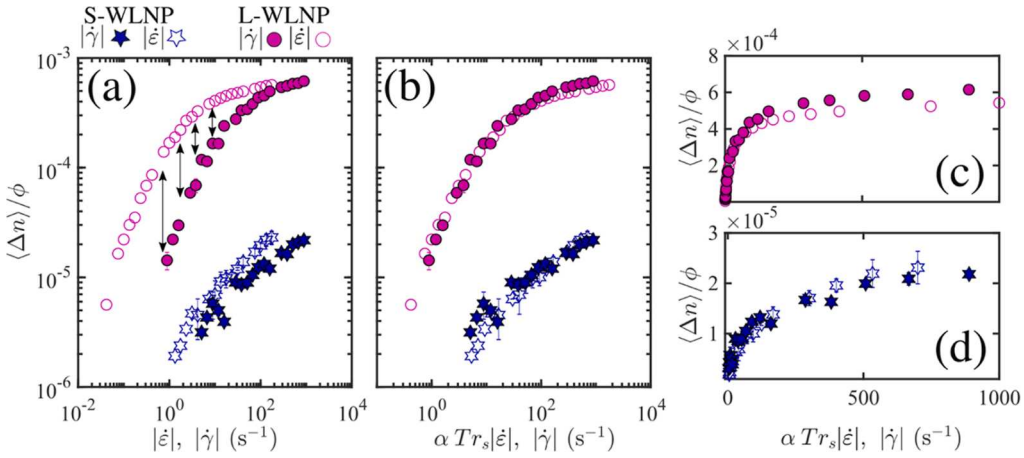

Figure 9. (a) Normalized mean birefringence, $\langle\Delta n\rangle/\phi$, obtained at specific locations of the SFC and OSCER as a function of the respective deformation rate (i.e., $|\dot{\varepsilon}|$ and $|\dot{\gamma}|$) for the L-WLNP and S-WLNP at $\phi = 66 \times 10^{-3}$ and $\phi = 72 \times 10^{-3}$, respectively. In (b), $|\dot{\varepsilon}|$ is scaled as $\alpha \mathrm{Tr}_s|\dot{\varepsilon}|$ where Tr_s is the Trouton ratio of the solvent fluid and α is an empirical scaling parameter. In (c,d), the double-linear plot for the L-WLNP and S-WLNP, respectively, as in (b).

log−log plot Figure 9b and a double linear plot in Figure 9c,d. This indicates that under flow, the S-WLNPs behave like rigid rods, whereas the L-WLNPs display a significant deviation from such behavior, as captured by $\alpha > 1$. A plausible explanation is that the shorter S-WLNPs are readily aligned under both shear and extensional flows, behaving essentially as rigid rods in both cases. In contrast, the longer L-WLNPs are 2.4× (i.e., $\alpha = 2.4$) more effectively aligned under extensional flow than shear flow when compared to rigid colloidal rods. We note that the scaling factor for $|\dot{\varepsilon}|$ is obtained by minimizing the sum of squared residuals between the two curves in Figure 9a (the detailed procedure is provided in the Supporting Information).

To better assess the physical interpretation of the α parameter in eq 8, it is instructive to evaluate the WLNP in terms of their extensibility. For soluble polymers, the extensibility is usually described by the finite extensibility parameter, $Le = l_c/\langle R^2\rangle^{1/2}$, which is the ratio of the polymer chain contour length, l_c, which corresponds to the maximum length achievable for the fully stretched chain, to its root-mean-squared end-to-end length at equilibrium, $\langle R^2\rangle^{1/2}$.[9,12] For rigid rod-like structures $Le \approx 1$, whereas for flexible polymer chains, $Le \gg 1$.[9,10] In the case of WLNP, the representative contour length $\langle l_c\rangle$ has been determined by TEM analysis. Using a worm-like chain model, $\langle R^2\rangle$ can be estimated using[52]

$$\langle R^2\rangle = 2l_p l_c - 2l_p^2(1 - \exp(-l_c/l_p)) \quad (9)$$

Using $l_p \approx 50$ nm and $l_c = \langle l_c\rangle$ in eq 9, we obtain $Le \approx 1.8$ and $Le = 2.7$, for the S-WLNP and L-WLNP, respectively. Thus, the longer L-WLNPs require more strain than the S-WLNPs to achieve the fully elongated conformation. The ratio of the contour length to the persistence length gives $\langle l_c\rangle/l_p = 14$ and $\langle l_c\rangle/l_p = 5$ for the L-WLNP and S-WLNP, respectively. This also suggests greater flexibility for the L-WLNP. Overall, our analysis suggests that α can be regarded as a structural parameter that contains useful information regarding the flexibility and extensibility of the WLNP. As such, direct comparison of the shear-induced versus extension-induced alignment can be used to capture the extent of flexibility through the α parameter in eq 8. A premise for the use of eq 8 to retrieve α is that the increase in birefringence as a function of $|\dot{\gamma}|$ is self-similar to the birefringence as a function $|\dot{\varepsilon}|$. Thus, these two curves can be collapsed onto a single master curve, as shown for the WLNP in Figure 9b, indicating that similar flow-induced structural changes occur during both shear and extension.

For the L-WLNP at low deformation rates, the birefringence obtained under extension is up to 1 order of magnitude greater than that under shear (see the arrows in Figure 9a). However, birefringence values obtained under shear and extension flows become similar at high deformation rates as the particles approach their maximum alignment (Figure 9a). Thus, in the limit of high deformation rates, the L-WLNPs approach their fully aligned state, and the difference between shear and extension for the L-WLNP alignment becomes negligible.[82]

As rheological and structural properties are linked, we evaluate the shear viscosity response of the WLNP dispersions with the extent of particle alignment under shear flow. To clearly visualize the WLNP alignment−rheology relationship, we plot the shear viscosity, $\eta(\dot{\gamma})$, in its normalized form, η/η_0, as a function of the birefringence, $\langle\Delta n\rangle/\phi$, obtained at the same shear rate (Figure 10a). The reduction in shear viscosity follows an exponential decay with the increasing $\langle\Delta n\rangle/\phi$ for both WLNPs, following a straight line in the semi-log representation given in Figure 10b,c. This alignment−rheology relationship suggests that a higher degree of WLNP alignment implies a

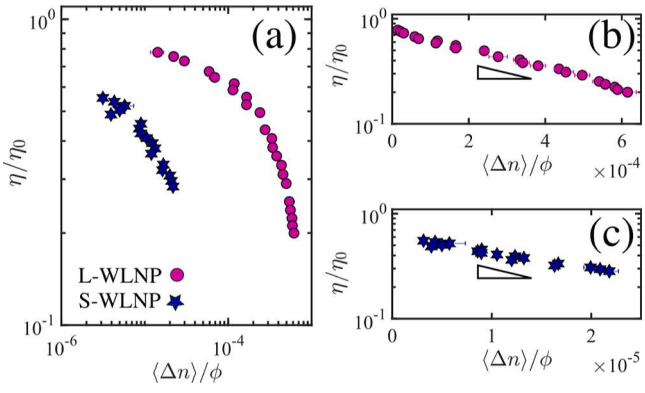

Figure 10. (a) Shear viscosity normalized as η/η_0 as a function of $\langle\Delta n\rangle/\phi$ for the L-WLNP and S-WLNP at $\phi = 66 \times 10^{-3}$ and $\phi = 72 \times 10^{-3}$, respectively. In (b,c), the semi-log representation for the L-WLNP and S-WLNP, respectively, as in (a).

https://doi.org/10.1021/acs.macromol.2c01314
Macromolecules 2022, 55, 10031−10042

lower dispersion viscosity. A similar exponential relationship between shear viscosity and particle alignment was also reported for rod-like viruses,[28,29] worm-like micelles, and block copolymer worms[27] via rheo-SAS experiments.

We propose that WLNP alignment under extensional-dominated flow produces an extensional-thinning response. This hypothesis is supported by three key observations: (i) the linear reduction of the fluid filament diameter over time ($2R_{mid}$ vs $t - t_0$ in Figure 6b) near the breakup time in the uniaxial extension experiment, which is in distinct contrast to the exponential decay observed for extensional-hardening fluids;[21] (ii) the lack of any detectable excess pressure drop ($\Delta P_{excess} = \Delta P_{total} - \Delta P_{shear} \approx 0$) within the OSCER device owing to comparable extensional stress and shear stress under such conditions (Figure 7); and (iii) the self-similar birefringence trends under shear flow and under extensional flow, indicating that an analogous structural mechanism operates in each case. In addition to points (i) and (ii), the fact that G'' exceeds G' over a wide range of angular frequency (see Figure 5e) provides further evidence that the elastic stress, arising from WLNP stretching (bending), and the entropic stress, owing to a reduction in the number of orientational configurations, must be small compared to the viscous stress.

CONCLUSIONS

We report the alignment and rheological behavior of two types of WLNPs under both shear and extensional flows. The shear-thinning behavior and a viscous-dominated response are observed under shear flow. Moreover, the complex modulus (G'') obtained as a function of the angular frequency for the S-WLNP and L-WLNP in the semi-dilute regime can be described by a concentration- and particle-independent master curve. Under extensional-dominated flow conditions, the WLNPs display a viscous-dominated response without any detectable elasticity. WLNP alignment follows a self-similar trend when subjected to either shear or extensional flow, with extensional forces proving to be more effective at inducing the onset of WLNP alignment than shear forces. To quantitatively capture this difference, we introduce a scaling factor (αTr_s) to the extension rate as $|\dot{\gamma}| = |\dot{\epsilon}|(\alpha Tr_s)$, where α is a dimensionless structural parameter related to the flexibility and extensibility of the particles and Tr_s is the Trouton ratio of the solvent (where $Tr_s = 4$ for planar extension). For the S-WLNP, the extensional deformation rate was 4 times more effective at inducing the onset of alignment than the shear deformation rate (with $\alpha = 1$), as previously shown experimentally for rigid rods.[15] Interestingly, the L-WLNP did not follow the behavior expected for rigid rods, and the extensional deformation rate was ~9.5 times more effective at inducing alignment than shear deformation rate (with $\alpha = 2.4$). Although the S-WLNPs are considered to be semi-flexible nanoparticles, FIB analysis suggested that they effectively behaved as rigid rods under flow. In contrast, the L-WLNPs were more efficiently stretched and aligned under extensional flow than under shear flow compared to the S-WLNP. The α parameter appears to correlate with the flexibility and extensibility of the WLNP and enables the relative effectiveness of extensional flow versus shear flow at inducing particle alignment to be captured. This suggests that the α parameter can serve as a useful index to infer the flexibility/extensibility of anisotropic colloidal particles based on their differing ability to induce birefringence under extensional and shear flow, respectively. The scaling analysis required to obtain α relies solely on the self-similar behavior of the birefringence under shear and extensional flow, without requiring any prior knowledge of the nanoparticle contour length or persistence length. In the future, it would be interesting to establish a more physically grounded interpretation of the α parameter by evaluating a library of WLNP, along with other rod-like nanoparticles of varying contour lengths and flexibility. Finally, we find that both types of WLNPs exhibit shear-thinning behavior, with the dispersion viscosity decaying exponentially with increasing WLNP alignment. Accordingly, we hypothesize that greater degrees of alignment under extensional flow cause extensional thinning. Compared to flexible polymer chains in solution, the WLNPs offer important advantages owing to their ability to tune the shear and extensional fluid viscosity by varying the WLNP concentration while avoiding difficulties related to flow instabilities and the stringiness/stickiness often associated with flexible polymer chains. Overall, the shear and extensional flow behavior reported herein suggest that these WLNPs may be used as additives for formulations that require jetting, spraying, and rapid, clean dispensing.

ASSOCIATED CONTENT

Supporting Information

The Supporting Information is available free of charge at https://pubs.acs.org/doi/10.1021/acs.macromol.2c01314.

Synthesis and characterization; shear rheology; and birefringence scaling (PDF)

AUTHOR INFORMATION

Corresponding Authors

Vincenzo Calabrese − *Okinawa Institute of Science and Technology, Onna-son, Okinawa 904-0495, Japan;* orcid.org/0000-0001-5974-9217; Email: vincenzo.calabrese@oist.jp

Amy Q. Shen − *Okinawa Institute of Science and Technology, Onna-son, Okinawa 904-0495, Japan;* orcid.org/0000-0002-1222-6264; Email: amy.shen@oist.jp

Authors

Csilla György − *Dainton Building, Department of Chemistry, The University of Sheffield, Sheffield, South Yorkshire S3 7HF, U.K..*

Simon J. Haward − *Okinawa Institute of Science and Technology, Onna-son, Okinawa 904-0495, Japan;* orcid.org/0000-0002-1884-4100

Thomas J. Neal − *Dainton Building, Department of Chemistry, The University of Sheffield, Sheffield, South Yorkshire S3 7HF, U.K..*

Steven P. Armes − *Dainton Building, Department of Chemistry, The University of Sheffield, Sheffield, South Yorkshire S3 7HF, U.K..;* orcid.org/0000-0002-8289-6351

Complete contact information is available at: https://pubs.acs.org/10.1021/acs.macromol.2c01314

Notes

The authors declare no competing financial interest.

ACKNOWLEDGMENTS

The authors gratefully acknowledge the support of Okinawa Institute of Science and Technology Graduate University with subsidy funding from the Cabinet Office, Government of Japan. V.C., S.J.H., and A.Q.S. also acknowledge the financial support

from the Japanese Society for the Promotion of Science (JSPS, grant nos. 22K14738, 18K03958, 18H01135, and 21K03884) and the Joint Research Projects (JRPs) supported by the JSPS and the Swiss National Science Foundation (SNSF). We thank the EPSRC for a CDT Ph.D. studentship for C.G. (EP/L016281) and Lubrizol Ltd. (Hazelwood, Derbyshire, UK) for the financial support of this project and for permission to publish these results. S.P.A. also acknowledges an EPSRC Established Career Particle Technology Fellowship (EP/R003009).

REFERENCES

(1) Doi, M. *Soft Matter Physics*; Oxford University Press, 2013.
(2) Nordenström, M.; Fall, A.; Nyström, G.; Wågberg, L. Formation of Colloidal Nanocellulose Glasses and Gels. *Langmuir* **2017**, *33*, 9772−9780.
(3) Lovett, J. R.; Derry, M. J.; Yang, P.; Hatton, F. L.; Warren, N. J.; Fowler, P. W.; Armes, S. P. Can percolation theory explain the gelation behavior of diblock copolymer worms? *Chem. Sci.* **2018**, *9*, 7138−7144.
(4) Doi, M.; Edwards, S. F.; Edwards, S. F. *The Theory of Polymer Dynamics*; Oxford University Press, 1988.
(5) Mewis, J.; Wagner, N. J. *Colloidal Suspension Rheology*; Cambridge University Press, 2012.
(6) Sogabe, A.; Matsuo, A.; Yusa, S.-i. Low-stringiness thickener and cosmetic material admixed with said thickener. U.S. Patent 20,180,036,221 A1, 15/784, 337, 2018.
(7) Trouton, F. T. On the coefficient of viscous traction and its relation to that of viscosity. *Proc. R. Soc. London, Ser. A* **1906**, *77*, 426−440.
(8) Petrie, C. J. S. Extensional viscosity: A critical discussion. *J. Non-Newtonian Fluid Mech.* **2006**, *137*, 15−23.
(9) Sharma, V.; Haward, S. J.; Serdy, J.; Keshavarz, B.; Soderlund, A.; Threlfall-Holmes, P.; McKinley, G. H. The rheology of aqueous solutions of ethyl hydroxy-ethyl cellulose (EHEC) and its hydrophobically modified analogue (hmEHEC): Extensional flow response in capillary break-up, jetting (ROJER) and in a cross-slot extensional rheometer. *Soft Matter* **2015**, *11*, 3251−3270.
(10) Dinic, J.; Sharma, V. Macromolecular relaxation, strain, and extensibility determine elastocapillary thinning and extensional viscosity of polymer solutions. *Proc. Natl. Acad. Sci. U.S.A.* **2019**, *116*, 8766−8774.
(11) Haward, S. J.; Oliveira, M. S. N.; Alves, M. A.; McKinley, G. H. Optimized Cross-Slot Flow Geometry for Microfluidic Extensional Rheometry. *Phys. Rev. Lett.* **2012**, *109*, 128301.
(12) Keshavarz, B.; McKinley, G. H. Micro-scale extensional rheometry using hyperbolic converging/diverging channels and jet breakup. *Biomicrofluidics* **2016**, *10*, 043502.
(13) Varchanis, S.; Hopkins, C. C.; Shen, A. Q.; Tsamopoulos, J.; Haward, S. J. Asymmetric flows of complex fluids past confined cylinders: A comprehensive numerical study with experimental validation. *Phys. Fluids* **2020**, *32*, 053103.
(14) De Gennes, P. G. Coil-stretch transition of dilute flexible polymers under ultrahigh velocity gradients. *J. Chem. Phys.* **1974**, *60*, 5030−5042.
(15) Calabrese, V.; Haward, S. J.; Shen, A. Q. Effects of shearing and extensional flows on the alignment of colloidal rods. *Macromolecules* **2021**, *54*, 4176−4185.
(16) Calabrese, V.; Varchanis, S.; Haward, S. J.; Tsamopoulos, J.; Shen, A. Q. Structure-property relationship of a soft colloidal glass in simple and mixed flows. *J. Colloid Interface Sci.* **2021**, *601*, 454−466.
(17) Lundahl, M. J.; Berta, M.; Ago, M.; Stading, M.; Rojas, O. J. Shear and extensional rheology of aqueous suspensions of cellulose nanofibrils for biopolymer-assisted filament spinning. *Eur. Polym. J.* **2018**, *109*, 367−378.
(18) Ng, H. C.-H.; Corker, A.; García-Tuñón, E.; Poole, R. J. GO CaBER: Capillary breakup and steady-shear experiments on aqueous graphene oxide (GO) suspensions. *J. Rheol.* **2020**, *64*, 81−93.
(19) Lang, C.; Hendricks, J.; Zhang, Z.; Reddy, N. K.; Rothstein, J. P.; Lettinga, M. P.; Vermant, J.; Clasen, C. Effects of particle stiffness on the extensional rheology of model rod-like nanoparticle suspensions. *Soft Matter* **2019**, *15*, 833−841.
(20) Ma, A. W.; Chinesta, F.; Tuladhar, T.; Mackley, M. R. Filament stretching of carbon nanotube suspensions. *Rheol. Acta* **2008**, *47*, 447−457.
(21) Haward, S. Microfluidic extensional rheometry using stagnation point flow. *Biomicrofluidics* **2016**, *10*, 043401.
(22) Mykhaylyk, O. O. Time-resolved polarized light imaging of sheared materials: Application to polymer crystallization. *Soft Matter* **2010**, *6*, 4430−4440.
(23) Mykhaylyk, O. O.; Chambon, P.; Impradice, C.; Fairclough, J. P. A.; Terrill, N. J.; Ryan, A. J. Control of structural morphology in shear-induced crystallization of polymers. *Macromolecules* **2010**, *43*, 2389−2405.
(24) Holland, C.; Vollrath, F.; Ryan, A. J.; Mykhaylyk, O. O. Silk and synthetic polymers: Reconciling 100 degrees of separation. *Adv. Mater.* **2012**, *24*, 105−109.
(25) Mykhaylyk, O. O.; Parnell, A. J.; Pryke, A.; Fairclough, J. P. A. Direct imaging of the orientational dynamics of block copolymer lamellar phase subjected to shear flow. *Macromolecules* **2012**, *45*, 5260−5272.
(26) Vermant, J.; Yang, H.; Fuller, G. G. Rheooptical determination of aspect ratio and polydispersity of nonspherical particles. *AIChE J.* **2001**, *47*, 790−798.
(27) Förster, S.; Konrad, M.; Lindner, P. Shear thinning and orientational ordering of Wormlike Micelles. *Phys. Rev. Lett.* **2005**, *94*, 017803.
(28) Lang, C.; Kohlbrecher, J.; Porcar, L.; Radulescu, A.; Sellinghoff, K.; Dhont, J. K. G.; Lettinga, M. P. Microstructural understanding of the length- and stiffness-dependent shear thinning in semidilute colloidal rods. *Macromolecules* **2019**, *52*, 9604−9612.
(29) Lang, C.; Kohlbrecher, J.; Porcar, L.; Lettinga, M. P. The connection between biaxial orientation and shear thinning for quasi-ideal rods. *Polymers* **2016**, *8*, 291.
(30) van der Linden, E.; Sagis, L.; Venema, P. Rheo-optics and food systems. *Curr. Opin. Colloid Interface Sci.* **2003**, *8*, 349−358.
(31) Kádár, R.; Spirk, S.; Nypelö, T. Cellulose Nanocrystal Liquid Crystal Phases: Progress and Challenges in Characterization Using Rheology Coupled to Optics, Scattering, and Spectroscopy. *ACS Nano* **2021**, *15*, 7931−7945.
(32) Trebbin, M.; Steinhauser, D.; Perlich, J.; Buffet, A.; Roth, S. V.; Zimmermann, W.; Thiele, J.; Förster, S. Anisotropic particles align perpendicular to the flow direction in narrow microchannels. *Proc. Natl. Acad. Sci. U.S.A.* **2013**, *110*, 6706−6711.
(33) Rosén, T.; Wang, R.; Zhan, C.; He, H.; Chodankar, S.; Hsiao, B. S. Cellulose nanofibrils and nanocrystals in confined flow: Single-particle dynamics to collective alignment revealed through scanning small-angle X-ray scattering and numerical simulations. *Phys. Rev. E* **2020**, *101*, 032610.
(34) Corona, P. T.; Ruocco, N.; Weigandt, K. M.; Leal, L. G.; Helgeson, M. E. Probing flow-induced nanostructure of complex fluids in arbitrary 2D flows using a fluidic four-roll mill (FFoRM). *Sci. Rep.* **2018**, *8*, 15559.
(35) Chiefari, J.; Chong, Y. K. B.; Ercole, F.; Krstina, J.; Jeffery, J.; Le, T. P. T.; Mayadunne, R. T. A.; Meijs, G. F.; Moad, C. L.; Moad, G.; Rizzardo, E.; Thang, S. H. Living Free-Radical Polymerization by Reversible Addition−Fragmentation Chain Transfer: The RAFT Process. *Macromolecules* **1998**, *31*, 5559−5562.
(36) Perrier, S. 50th Anniversary Perspective: RAFT Polymerization-A User Guide. *Macromolecules* **2017**, *50*, 7433−7447.
(37) György, C.; Verity, C.; Neal, T. J.; Rymaruk, M. J.; Cornel, E. J.; Smith, T.; Growney, D. J.; Armes, S. P. RAFT Dispersion Polymerization of Methyl Methacrylate in Mineral Oil: High Glass Transition Temperature of the Core-Forming Block Constrains the Evolution of Copolymer Morphology. *Macromolecules* **2021**, *54*, 9496−9509.
(38) György, C.; Derry, M. J.; Cornel, E. J.; Armes, S. P. Synthesis of Highly Transparent Diblock Copolymer Vesicles via RAFT Dispersion Polymerization of 2,2,2-Trifluoroethyl Methacrylate in n-Alkanes. *Macromolecules* **2021**, *54*, 1159−1169.

(39) Derry, M. J.; Mykhaylyk, O. O.; Armes, S. P. Shear-induced alignment of block copolymer worms in mineral oil. *Soft Matter* **2021**, *17*, 8867−8876.
(40) Trent, J. S. Ruthenium Tetraoxide Staining of Polymers: New Preparative Methods for Electron Microscopy. *Macromolecules* **1984**, *17*, 2930−2931.
(41) Pauw, B. R.; Smith, A. J.; Snow, T.; Terrill, N. J.; Thünemann, A. F. The modular small-angle X-ray scattering data correction sequence. *J. Appl. Crystallogr.* **2017**, *50*, 1800−1811.
(42) Ilavsky, J.; Jemian, P. R. Irena: tool suite for modeling and analysis of small-angle scattering. *J. Appl. Crystallogr.* **2009**, *42*, 347−353.
(43) Campo-Deaño, L.; Clasen, C. The slow retraction method (SRM) for the determination of ultra-short relaxation times in capillary breakup extensional rheometry experiments. *J. Non-Newtonian Fluid Mech.* **2010**, *165*, 1688−1699.
(44) Calabrese, V.; Varchanis, S.; Haward, S. J.; Shen, A. Q. Alignment of Colloidal Rods in Crowded Environments. *Macromolecules* **2022**, *55*, 5610−5620.
(45) Haward, S. J.; McKinley, G. H.; Shen, A. Q. Elastic instabilities in planar elongational flow of monodisperse polymer solutions. *Sci. Rep.* **2016**, *6*, 33029.
(46) Haward, S. J.; Toda-Peters, K.; Shen, A. Q. Steady viscoelastic flow around high-aspect-ratio, low-blockage-ratio microfluidic cylinders. *J. Non-Newtonian Fluid Mech.* **2018**, *254*, 23−35.
(47) Qi, J.; Elson, D. S. Mueller polarimetric imaging for surgical and diagnostic applications: a review. *J. Biophotonics* **2017**, *10*, 950−982.
(48) Pedersen, J. S. Form factors of block copolymer micelles with spherical, ellipsoidal and cylindrical cores. *J. Appl. Crystallogr.* **2000**, *33*, 637−640.
(49) Usov, I.; Mezzenga, R. FiberApp: An open-source software for tracking and analyzing polymers, filaments, biomacromolecules, and fibrous objects. *Macromolecules* **2015**, *48*, 1269−1280.
(50) De Gennes, P. G. *Scaling Concepts in Polymer Physics*; Cornell University Press, 1979.
(51) Lang, C.; Lettinga, M. P. Shear flow behavior of bidisperse rodlike colloids. *Macromolecules* **2020**, *53*, 2662−2668.
(52) Rubinstein, M.; Colby, R. H.; et al. *Polymer Physics*; Oxford University Press: New York, 2003.
(53) Ebagninin, K. W.; Benchabane, A.; Bekkour, K. Rheological characterization of poly(ethylene oxide) solutions of different molecular weights. *J. Colloid Interface Sci.* **2009**, *336*, 360−367.
(54) Potier, M.; Tea, L.; Benyahia, L.; Nicolai, T.; Renou, F. Viscosity of aqueous polysaccharide solutions and selected homogeneous binary mixtures. *Macromolecules* **2020**, *53*, 10514−10525.
(55) Snijkers, F.; Vlassopoulos, D. Appraisal of the Cox-Merz rule for well-characterized entangled linear and branched polymers. *Rheol. Acta* **2014**, *53*, 935−946.
(56) Rathinaraj, J. D. J.; Keshavarz, B.; McKinley, G. H. Why the Cox-Merz rule and Gleissle mirror relation work: A quantitative analysis using the Wagner integral framework with a fractional Maxwell kernel. *Phys. Fluids* **2022**, *34*, 033106.
(57) Ureña-Benavides, E. E.; Ao, G.; Davis, V. A.; Kitchens, C. L. Rheology and Phase Behavior of Lyotropic Cellulose Nanocrystal Suspensions. *Macromolecules* **2011**, *44*, 8990−8998.
(58) Bertsch, P.; Isabettini, S.; Fischer, P. Ion-induced hydrogel formation and nematic ordering of nanocrystalline cellulose suspensions. *Biomacromolecules* **2017**, *18*, 4060−4066.
(59) Cross, M. M. Rheology of synthetic latices: Influence of shear rate and temperature. *J. Colloid Interface Sci.* **1973**, *44*, 175−176.
(60) Dhont, J. K.; Briels, W. J. Viscoelasticity of suspensions of long, rigid rods. *Colloids Surf., A* **2003**, *213*, 131−156.
(61) Krieger, I. M.; Dougherty, T. J. A Mechanism for Non-Newtonian Flow in Suspensions of Rigid Spheres. *Trans. Soc. Rheol.* **1959**, *3*, 137−152.
(62) Einstein, A. Berichtigung zu meiner Arbeit: "Eine neue Bestimmung der Moleküldimensionen". *Ann. Phys.* **1911**, *339*, 591−592.
(63) Santamaría-Holek, I.; Mendoza, C. I. The rheology of concentrated suspensions of arbitrarily-shaped particles. *J. Colloid Interface Sci.* **2010**, *346*, 118−126.
(64) Simha, R. The influence of Brownian movement on the viscosity of solutions. *J. Phys. Chem.* **1940**, *44*, 25−34.
(65) Iwamoto, S.; Lee, S. H.; Endo, T. Relationship between aspect ratio and suspension viscosity of wood cellulose nanofibers. *Polymer J.* **2014**, *46*, 73−76.
(66) Larson, R. G.; Ottinger, H. C. Effect of Molecular Elasticity on Out-of-Plane Orientations in Shearing Flows of Liquid-Crystalline Polymers. *Macromolecules* **1991**, *24*, 6270−6282.
(67) Colby, R. H. Structure and linear viscoelasticity of flexible polymer solutions: Comparison of polyelectrolyte and neutral polymer solutions. *Rheol. Acta* **2010**, *49*, 425−442.
(68) Dinic, J.; Sharma, V. Power Laws Dominate Shear and Extensional Rheology Response and Capillarity-Driven Pinching Dynamics of Entangled Hydroxyethyl Cellulose (HEC) Solutions. *Macromolecules* **2020**, *53*, 3424−3437.
(69) Fujii, S.; Sasaki, N.; Nakata, M. Phenomenological analysis of elongational flow birefringence in semidilute solutions of hydroxypropylcellulose. *Colloid Polym. Sci.* **2003**, *281*, 823−831.
(70) Del Giudice, F.; Tassieri, M.; Oelschlaeger, C.; Shen, A. Q. When Microrheology, Bulk Rheology, and Microfluidics Meet: Broadband Rheology of Hydroxyethyl Cellulose Water Solutions. *Macromolecules* **2017**, *50*, 2951−2963.
(71) Haward, S. J.; Sharma, V.; Butts, C. P.; McKinley, G. H.; Rahatekar, S. S. Shear and extensional rheology of cellulose/ionic liquid solutions. *Biomacromolecules* **2012**, *13*, 1688−1699.
(72) McKinley, G. H.; Tripathi, A. How to extract the Newtonian viscosity from capillary breakup measurements in a filament rheometer. *J. Rheol.* **2000**, *44*, 653−670.
(73) Varchanis, S.; Makrigiorgos, G.; Moschopoulos, P.; Dimakopoulos, Y.; Tsamopoulos, J. Modeling the rheology of thixotropic elasto-visco-plastic materials. *J. Rheol.* **2019**, *63*, 609−639.
(74) Haward, S. J.; Ober, T. J.; Oliveira, M. S.; Alves, M. A.; McKinley, G. H. Extensional rheology and elastic instabilities of a wormlike micellar solution in a microfluidic cross-slot device. *Soft Matter* **2012**, *8*, 536−555.
(75) Haward, S. J.; Sharma, V.; Odell, J. A. Extensional opto-rheometry with biofluids and ultra-dilute polymer solutions. *Soft Matter* **2011**, *7*, 9908−9921.
(76) Reddy, N. K.; Natale, G.; Prud'homme, R. K.; Vermant, J. Rheo-optical analysis of functionalized graphene suspensions. *Langmuir* **2018**, *34*, 7844−7851.
(77) Qazi, S. J. S.; Rennie, A. R.; Tucker, I.; Penfold, J.; Grillo, I. Alignment of Dispersions of Plate-Like Colloidal Particles of Ni(OH)-2Induced by Elongational Flow. *J. Phys. Chem. B* **2011**, *115*, 3271−3280.
(78) Xin, G.; Zhu, W.; Deng, Y.; Cheng, J.; Zhang, L. T.; Chung, A. J.; De, S.; Lian, J. Microfluidics-enabled orientation and microstructure control of macroscopic graphene fibres. *Nat. Nanotechnol.* **2019**, *14*, 168−175.
(79) Haward, S. J. Characterization of hyaluronic acid and synovial fluid in stagnation point elongational flow. *Biopolymers* **2014**, *101*, 287−305.
(80) Keller, A.; Odell, J. A. The extensibility of macromolecules in solution; A new focus for macromolecular science. *Colloid Polym. Sci.* **1985**, *263*, 181−201.
(81) Del Giudice, F.; Haward, S. J.; Shen, A. Q. Relaxation time of dilute polymer solutions: A microfluidic approach. *J. Rheol.* **2017**, *61*, 327−337.
(82) Liu, Y.; Zografos, K.; Fidalgo, J.; Duchêne, C.; Quintard, C.; Darnige, T.; Filipe, V.; Huille, S.; du Roure, O.; Oliveira, M. S.; et al. Optimised hyperbolic microchannels for the mechanical characterisation of bio-particles. *Soft Matter* **2020**, *16*, 9844−9856.

https://doi.org/10.1021/acs.macromol.2c01314
Macromolecules 2022, 55, 10031−10042